Article | Open Access

Energy Materials

Lee *et al. Energy Mater.* **2026**, *6*, 600120 **DOI:**10.20517/energymater.2026.161

CsCl interface-driven structural resilience of $FAPbI_3$ to humidity

Gun-Hee Lee, Hui-Seon Kim*

Keywords:
Perovskite solar cell, $FAPbI_3$, CsCl, moisture stability, structural resilience, phase recovery

Citation: Lee, G. H.; Kim, H. S. CsCl interface-driven structural resilience of $FAPbI_3$ to humidity. *Energy Mater.* **2026**, *6*, 600120. https://dx.doi.org/10.20517/energymater.2026.161

Received: 8 Jun 2026
First Decision: 29 Jun 2026
Revised: 29 Jul 2026
Accepted: 11 Aug 2026
Published: 18 Sep 2026

Academic Editor:
Sining Yun
Copy Editor:
Ping Zhang
Production Editor:
Ping Zhang

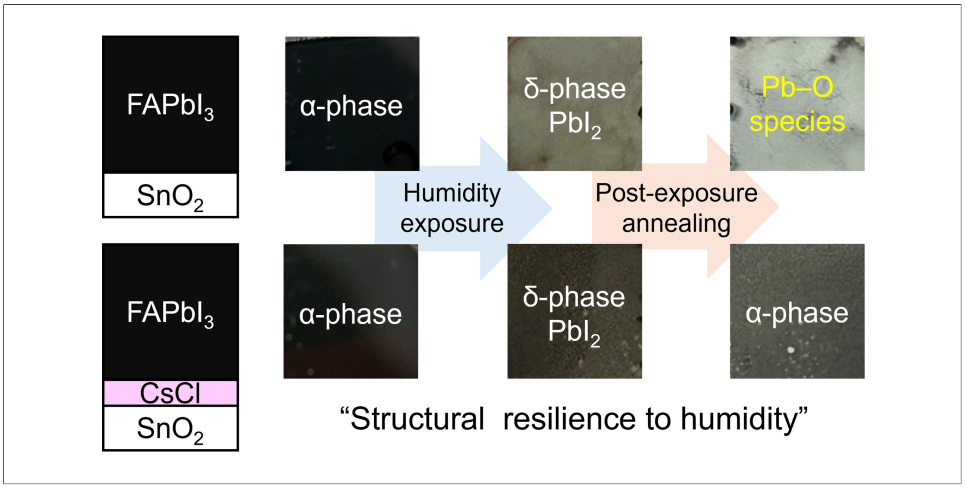

Abstract

Despite their power conversion efficiencies reaching 28.0%, formamidinium lead iodide ($FAPbI_3$)-based perovskite solar cells (PSCs) suffer from moisture-induced phase degradation that initiates preferentially at the SnO_2/$FAPbI_3$ buried interface, yet the coupling between humidity exposure and thermal stress at the interface remains unclear. Here, we introduce a CsCl interlayer at the buried interface of n-i-p-structured PSCs and examine its role in reinforcing the structural resilience of $FAPbI_3$ against moisture at elevated temperature. This interfacial role is distinguished from the improved crystallinity of the pristine $FAPbI_3$ film that CsCl is already known to provide. The CsCl interlayer blocked the irreversible formation of Pb-O-related species and enabled partial reconversion of the moisture-driven δ-phase and PbI_2 back to the α-phase during post-exposure annealing. Sequential changes in the lattice bonding environment across the pristine, humidity-exposed, and post-exposure annealed films were analyzed by complementary X-ray diffraction, grazing-incidence X-ray diffraction, Fourier-transform infrared spectroscopy, and X-ray photoelectron spectroscopy to elucidate the CsCl interlayer-induced stabilization mechanism in $FAPbI_3$.

Department of Chemistry and Chemical Engineering, Inha University, Incheon 22212, Republic of Korea.

***Correspondence to:** Prof. Hui-Seon Kim, Department of Chemistry and Chemical Engineering, Inha University, Incheon 22212, Republic of Korea. E-mail: hui-seon.kim@inha.ac.kr

INTRODUCTION

Remarkable progress has been made in perovskite solar cells (PSCs) since the first report of all-solid-state PSCs in 2012[1], with certified power conversion efficiencies (PCEs) reaching 28.0% in 2026[2]. Formamidinium lead iodide ($FAPbI_3$) perovskites have emerged as leading photoactive compositions[3], owing to their near-ideal bandgap[4], strong light harvesting[5], high defect tolerance dominated by shallow trap states[6], and effective dielectric screening of charge carriers arising from the soft lattice, which ensures long carrier diffusion lengths and lifetimes[7]. Despite these favorable optoelectronic properties, the structural instability of the perovskite phase remains a persistent challenge for halide perovskite materials[6]. $FAPbI_3$ is intrinsically susceptible to moisture[8], undergoing several decomposition pathways: the α-to-δ phase transition (to a yellow, photoinactive phase)[9], decomposition into PbI_2 and formamidinium iodide (FAI)[10], loss of the organic FA^+ cation[11], and the formation of iodine-related defects[12]. Moreover, the interplay between perovskite defects near the buried interface and surface defects of the underlying metal oxide (e.g., SnO_2) has been shown to initiate perovskite degradation[13,14], leading to severe performance loss and compromised long-term stability. SnO_2 is among the most widely used electron transport layers in n-i-p-structured PSCs, owing to its high transparency, excellent electron mobility, low-temperature processability, and favorable band alignment with the perovskite absorber[15]. However, the SnO_2 surface contains a variety of defects and adsorbates - including oxygen vacancies, hydroxyl groups, dangling bonds, and chemisorbed oxygen - which can accelerate both nonradiative recombination and moisture-induced interfacial degradation[14]. Vacancy-related defects are common in solution-processed SnO_2 and create reactive interfacial sites for water molecules under environmental stress[14,16,17]. Oxygen vacancies in SnO_{2-x}, promoted by adsorbed H_2O, raise the positive charge density on neighboring Sn atoms and thereby elongate and weaken the interfacial Pb-I bond. The weakened bonding accelerates interfacial ion migration and ultimately drives phase decomposition[12,18,19]. This destabilized bonding environment lowers the barrier for iodine interstitial formation and promotes the diffusion of iodine-related defects into the defect-rich SnO_2. Furthermore, oxygen-deficient SnO_2 thermally activates oxygen migration[20], and an applied electric bias further drives the release and redistribution of oxygen-related species from SnO_2 toward the perovskite, aggravating interfacial instability[21]. Oxygen vacancies can additionally serve as bonding sites for A-site cations in halide perovskites ($APbX_3$; A^+ = monovalent cation and X^- = halide)[22]. The resulting structural distortion, combined with FAI deprotonation and iodine-defect generation, favors transitions from the photoactive α-phase to non-photoactive δ-$FAPbI_3$, PbI_2, and other secondary phases[22,23]. Interface engineering of the SnO_2/$FAPbI_3$ buried interface is therefore critical to phase stability of perovskite[16], suppressing the defect-mediated degradation pathways. In this regard, various interfacial engineering strategies have been reported to suppress defects at the buried interface[24-26]. In particular, alkali halides have been widely employed as interlayers at metal oxide/perovskite interfaces[24,27,28]. One of the most common interlayers based on alkali halides is KCl, which effectively passivates interfacial defects to suppress charge recombination and simultaneously regulates crystallization of perovskite films[27]. Similarly, CsCl has been employed either as an interlayer at the buried interface or as an additive in the perovskite precursor[29-31]. CsCl as an interlayer was found to improve the resistance of methylammonium lead iodide ($MAPbI_3$) to ultraviolet light and to enhance the moisture stability of $FAPbI_3$ by reducing the microstrain of the overlying perovskite film[32,33]. In addition, CsCl has been widely employed as an additive in the perovskite precursor solution, where the partial substitution of FA^+ by smaller Cs^+ cations introduces beneficial lattice strain and thereby stabilizes α-phase[33]. The phase-stabilizing role of CsCl in $FAPbI_3$ has been attributed to Cs^+-induced contraction of the octahedral cages and modification of the Pb-I bonding environment, which relieves the excess lattice strain of pristine $FAPbI_3$[22]. The accompanying strengthening of the Pb-I framework raises the thermodynamic stability of the α-phase and lowers the δ-to-α transition temperature[18,20]. The improved moisture resistance reported for $FAPbI_3$ films deposited on a CsCl interlayer has likewise been rationalized within this framework[21,33]. CsCl has thus been reported to be effective both as an interlayer and as a precursor additive, although its role has largely been limited to lattice stabilization and/or improved

crystallinity of perovskite films.

In this study, we focus instead on the structural resilience of $FAPbI_3$ grown on a SnO_2 layer, examining how the α-phase recovers after moisture-induced decomposition in the presence of a CsCl interlayer and separating this interfacial effect from phase stabilization within the bulk $FAPbI_3$ film. Structural resilience, defined here as the recovery of the α-phase lattice following stress-induced degradation, is therefore distinct from the phase stability or the degradation itself that previous reports have mainly addressed. Here we introduced a CsCl interlayer at the SnO_2/$FAPbI_3$ buried interface of n-i-p-structured PSCs to mitigate the coupling effect of moisture- and thermal stress-driven phase degradation originating at this buried interface. We systematically examined how the CsCl interlayer reinforces the humidity resilience of α-phase by stabilizing the vulnerable SnO_2/$FAPbI_3$ buried interface, taking into account the coupled contributions of the underlying SnO_2 substrate and the overlying $FAPbI_3$ to phase stability against moisture. Beyond the well-known reversible α-to-δ transition, $FAPbI_3$ exposed to 82%-88% relative humidity (RH) underwent irreversible decomposition to Pb-O-related species upon post-exposure annealing. The CsCl interlayer suppressed formation of both oxygen- and iodine-related defects at the buried interface, allowing the post-exposure annealing to partially recover the α-phase from the δ-phase and PbI_2 with retained FA^+.

EXPERIMENTAL

Chemicals

Synthesis of FAI: first, 80 mL of hydroiodic acid (57 wt% in H_2O, 99.99% Sigma-Aldrich) was added dropwise to 40 g of formamidine acetate salt (99%, Sigma-Aldrich) in a round-bottom flask for 1 h in an ice bath. The mixture was stirred at 300 rpm for 2 h at 0-5 °C and then evaporated to remove residual reactants. Then the product was dissolved in a small amount of pure ethanol (99.9%, Daejung) at 50 °C. After cooling down, the solution was dropped into ethyl ether (99.0%, Samchun) for recrystallization of FAI. This process was repeated five times for pure FAI salt. The product was washed with diethyl ether and dried at 50 °C overnight in a vacuum oven to remove residual solvent. Formamidinium bromide (FABr) salt was synthesized by the same method, except that hydroiodic acid was replaced with hydrobromic acid (48%, Sigma-Aldrich).

Preparation of a perovskite precursor

To prepare 1.5 M PbI_2 stock, PbI_2 beads (ultradry, 99.999%, Alfa Aesar) were dissolved in a mixed solvent of N,N-dimethylformamide (anhydrous, 99.8%, Sigma-Aldrich) and dimethyl sulfoxide (anhydrous, 99.9%, Sigma-Aldrich) with a 4:1 volume ratio. The PbI_2 stock solution was sonicated for 15 min, followed by annealing at 130 °C to ensure complete dissolution. To prepare 1.376 M $FAPbI_3$ solution, the PbI_2 stock solution was mixed with FAI salt using 9 mol% excess stoichiometry. Furthermore, methylenediamine dihydrochloride ($MDACl_2$, 98%, Sigma-Aldrich) and methylamine hydrochloride (MACl, 98%, Sigma-Aldrich) were added to the $FAPbI_3$ precursor to achieve a $FAPbI_3$:$MDACl_2$:MACl mol ratio of 1:0.038:0.35.

Device preparation

Fluorine-doped tin oxide (FTO) glass (≤ 8 ohm/sq, Pilkington) was used as the transparent conductive oxide (TCO) substrate. The substrates were sequentially sonicated in neutral detergent, distilled water, ethanol (70.0%-75.0%, Samchun), and acetone (Daejung) for 15 min each. For the electron transport layer, a SnO_2 colloidal solution (15% in H_2O, Alfa Aesar) was diluted to 4 wt% using deionized water. The diluted solution (80 μL) was dropped onto an FTO substrate subjected to UV-ozone (UVO) treatment for 15 min. The substrate was then spin-coated at 4,000 rpm for 20 s, followed by soft annealing at 80 °C. After 10 min, the SnO_2-coated FTO substrates were annealed in a furnace at 180 °C for 30 min. For the CsCl interlayer, cesium chloride (99%, Sigma-Aldrich) was dissolved in a mixed solvent of 2-propanol (99.5%, Sigma-Aldrich) and

deionized water with a 3:2 volume ratio. Cesium chloride (99%, Sigma-Aldrich), sodium chloride (99.5%, TCI), potassium chloride (99.999%, Sigma-Aldrich), and cesium iodide (99.999%, Sigma-Aldrich) were used as the interlayer materials. Then, 80 μL of CsCl solution was dynamically coated onto the UVO-treated substrates, followed by annealing at 100 °C for 10 min. After cooling, the substrates were treated with UVO for 15 min and transferred into an N_2-filled glovebox immediately before coating the perovskite solution. Next, 50 μL of the perovskite precursor was spin-coated at 5,000 rpm for 25 s, and 200 μL of chlorobenzene (99.5%, Daejung) was used as the antisolvent, dropped 5 s before the end of the program. The perovskite-coated substrate was annealed at 150 °C for 20 min. For the top surface treatment, 30 mM FABr was dissolved in 2-propanol. Then, 30 μL of FABr solution was coated onto the spinning substrate at 4,500 rpm for 20 s, followed by annealing at 100 °C for 10 min. Subsequently, 2,2',7,7'-tetrakis[*N*,*N*-di(4-methoxyphenyl)amino]-9,9'-spirobifluorene (spiro-OMeTAD, Luminescence Technology Corp.) was dissolved in chlorobenzene (99.8%, Sigma-Aldrich) at a concentration of 59 mM. After complete dissolution, 4-*tert*-butylpyridine (tBP, 98%, Sigma-Aldrich) and 1.8 M lithium bis(trifluoromethanesulfonyl)imide (Li-TFSI, 99.95%, Sigma-Aldrich) stock solution in acetonitrile (99.5%, TCI) were added at a molar ratio of 1:3.3:0.5 (spiro-OMeTAD:tBP:Li-TFSI) for the hole transport layer. The spiro-OMeTAD solution was dynamically coated on FABr-treated substrates at 4,500 rpm. Finally, an Ag electrode was thermally evaporated to a thickness of 100 nm.

Characterizations

Current density-voltage (J-V) measurements were performed under an AM 1.5G 100 mW/cm^2 Xe light source. Before the measurements, the light source was calibrated using a National Renewable Energy Laboratory (NREL)-certified Si solar cell with a KG5 filter. A solar simulator (model K730, McScience) was coupled with a source measurement unit (model 2400, Keithley). An aperture mask was used to define an active area of 0.16 cm^2. The J-V curves were obtained at a voltage sweep rate of 100 mV/s. Electrochemical impedance spectroscopy (EIS) measurements were performed using an SP-300 system (SN 1271, BioLogic) with a light-emitting diode light source (5,600 K). An alternating current perturbation of 20 mV was applied to direct current bias voltages of 0.3, 0.6, 0.7, 0.75, 0.8, 0.85, 0.9, 0.95, 1.0, and 1.1 V over a frequency range from 1 MHz to 0.1 Hz. For the equivalent circuit model, a series resistance connected with two parallel resistance-capacitance (RC) elements in series was used. X-ray diffraction (XRD) analysis was performed using an XPERT-PRO diffractometer system, and grazing-incidence X-ray diffraction (GIXRD) analysis was carried out using a SmartLab system (Rigaku). GIXRD was performed with the X-ray generator operated at 45 kV and 200 mA, using a D/teX Ultra 250 detector in continuous scan mode with a step size of 0.0001° and a fixed grazing incidence angle (ω) of 1°. For the $\sin^2\Psi$ analysis, the sample tilt angle (Ψ) was varied from 10° to 40°, and a diffraction profile was collected over a 2θ range of 30°-34° at each Ψ. Fourier-transform infrared (FT-IR) spectroscopy was performed using a PerkinElmer spectrometer over a range of 700-4,500 cm^{-1}. For depth-profile analysis, X-ray photoelectron spectroscopy (XPS, K-Alpha, Thermo Fisher Scientific) was conducted using an Ar^+ ion beam at 3 keV. Scanning electron microscopy (SEM) images were obtained using an SU-8230 system (Hitachi). Time-of-flight secondary ion mass spectrometry (ToF-SIMS) depth profiling and 3D imaging were performed on a TOF-SIMS M6 instrument (IONTOF GmbH, Münster, Germany) in negative-ion mode. Analysis used a 30 keV Bi_3^{2+} primary ion beam at approximately 0.5 pA, and sputtering was performed with a 2 keV Cs^+ beam at ~50 nA. An electron flood gun provided charge compensation.

RESULTS AND DISCUSSION

A CsCl interlayer was employed at the SnO_2/$FAPbI_3$ buried interface in n-i-p (SnO_2/$FAPbI_3$/spiro-OMeTAD)-structured PSCs, with the CsCl solution concentration varying from 10-90 mM [Figure 1 and Supplementary Figure 1]. Devices without the CsCl interlayer, hereafter referred to as the control, were compared with the CsCl-treated counterparts. The short-circuit photocurrent density (J_{SC}) was largely independent of CsCl treatment [Figure 1B and Supplementary Figure 1B], indicating that the CsCl interlayer

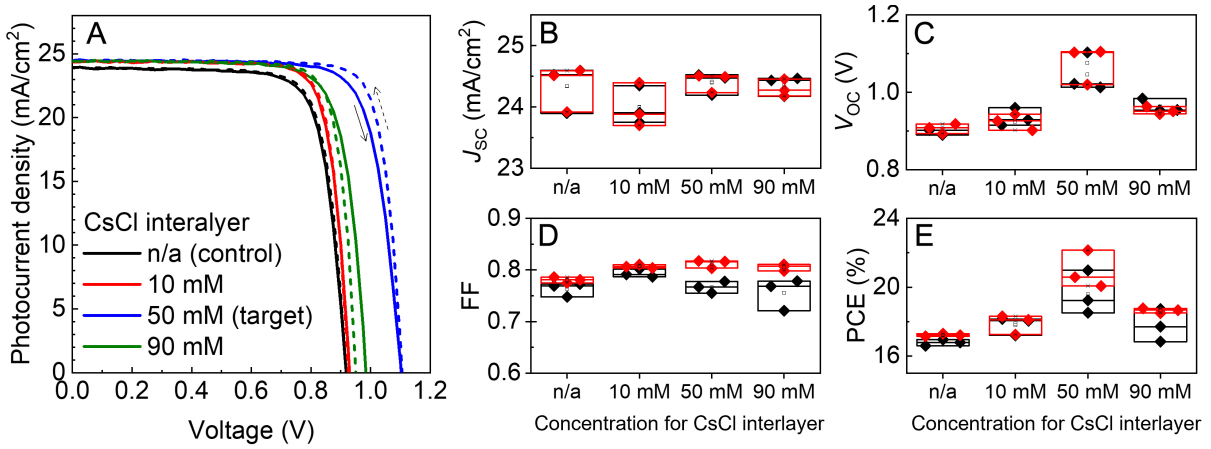

Figure 1. (A) Photocurrent density-voltage (J-V) curves of the champion devices as a function of the CsCl concentration. Statistical box plots of the photovoltaic parameters (B) J_{SC}, (C) V_{OC}, (D) fill factor (FF), and (E) PCE of PSCs with varying concentrations of CsCl. J-V curves and box plots of the photovoltaic parameters for devices with an active area of 0.16 cm². Black and red symbols in (B-E) denote the values obtained from forward and reverse scans, respectively. PCE: Power conversion efficiencie; PSCs: perovskite solar cells; J_{SC}: short-circuit photocurrent density; V_{OC}: open-circuit voltage.

has little effect on the light-harvesting efficiency of the perovskite layer. Peak performance was reached at 50 mM, which is taken as the target condition hereafter. The target device delivered the highest open-circuit voltage (V_{OC}) of 1.105 V, against 0.918 V for the control device [Figure 1C and Supplementary Figure 1C], and the best PCE increase from 17.15% for the control device to 22.15% for the target device [Figure 1E and Supplementary Figure 1E]. The stabilized power outputs of the control and target devices [Supplementary Figure 2] support the PCE gain from the CsCl interlayer. The higher V_{OC} and maximum-power-point voltage (V_{mpp}) of the target devices reflected suppressed nonradiative recombination at the interface, as evidenced by the largest recombination resistance (R_{rec}) over the CsCl concentration range of 10-90 mM [Supplementary Figure 3]. The voltage-dependent R_{rec} is shown in Supplementary Figure 3A by fitting the Nyquist plots [Supplementary Figures 3B-E] to an equivalent circuit. The low-frequency semi-arc is commonly assigned to defect-mediated recombination at the perovskite interface[34], indicating that CsCl passivates surface defects acting as recombination centers on both the SnO_2 and $FAPbI_3$ surfaces. Cl^- ions released from the CsCl interlayer likely coordinate with undercoordinated Pb^{2+} and halide vacancies on the $FAPbI_3$ side and with oxygen-related defects on the SnO_2 side[35,36]. Both interactions lower the overall interfacial defect density and suppress the defect-mediated charge recombination at the buried interface. The beneficial effect of the CsCl passivation is also evident in the long-term shelf stability test, where the photovoltaic performance of the target devices was better maintained over 2,000 h of dark storage than that of the control devices [Supplementary Figure 4].

The effect of CsCl-treated SnO_2 substrates on the crystal growth of $FAPbI_3$ was then examined by XRD. XRD patterns of the control and target perovskite films are shown in Figure 2A. Both perovskite films grew preferentially along the (001)/(002) direction, with a higher (001) intensity observed for the target film. The stronger preferential orientation indicates improved charge extraction along the vertically aligned $[PbI_6]^{4-}$ framework and fewer defects from reduced structural disorder[37], consistent with higher R_{rec} of the target devices[38]. The perovskite film crystallinity is generally governed by nucleation and growth kinetics, both of which depend on the underlying interfacial chemistry. Alkali halide interlayers such as KCl have been shown to slow crystallization through interactions between perovskite precursors and ions released from the interlayer[39,40]. Likewise, Cl^- transiently coordinates with Pb^{2+} during crystallization, favoring oriented growth. This enhanced structural orientation is also reflected in film morphology. The grain size distributions of the control and target films are compared in Figure 2B, where the target film produced larger grains. Although

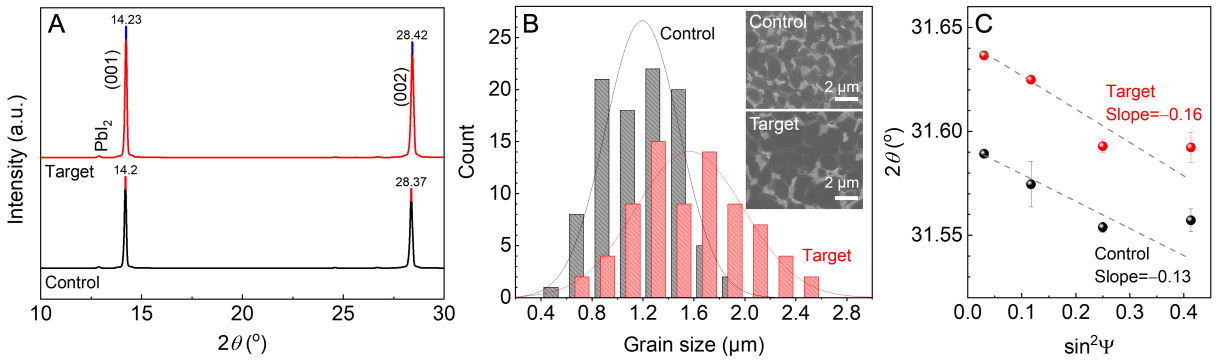

Figure 2. (A) XRD patterns and (B) grain-size distribution histograms of the control (black) and target (red) perovskite films. Insets in (B) show top-view SEM images of the control and target films; (C) 2θ-$\sin^2\Psi$ plots of the control (black) and target (red) films obtained by GIXRD. Error bars represent the standard error of the fitted peak positions from a single measurement. XRD: X-ray diffraction; SEM: scanning electron microscopy; GIXRD: grazing-incidence X-ray diffraction.

the coverage of the extremely thin CsCl interlayer is difficult to confirm directly, the uniform morphology and full coverage of the overlying perovskite films [Supplementary Figure 5] suggest that the CsCl interlayer is uniformly distributed, although this evidence is indirect. Grain size increased with CsCl concentration up to 50 mM and then mostly saturated at 90 mM [Supplementary Figures 5 and 6]. The (001) diffraction peak shifted slightly from 14.20° in the control film to 14.23° in the target film. This shift toward higher angle reflects lattice contraction, consistent with the incorporation of Cs^+ released from CsCl into the perovskite lattice during crystal growth[33]. To probe the depth dependence of this contraction, GIXRD patterns were collected at tilt angles (Ψ) between 10° and 40° [Supplementary Figure 7], where larger Ψ reflects crystallographic information from greater depths beneath the top surface. The corresponding 2θ-$\sin^2\Psi$ plot is shown in Figure 2C, where the target film shows a consistently higher 2θ than the control across the full Ψ range, reflecting the reduced lattice spacing that follows from substitution of FA^+ by the smaller Cs^+[41,42]. This confirms that lattice contraction persists throughout the film depth and indicates that Cs^+ diffusion toward the top surface was facilitated during crystal growth. The depth-independent contraction, on the other hand, had little effect on the residual lattice strain of the bulk perovskite, as reflected by comparable slope of the 2θ-$\sin^2\Psi$ plot[43]. Both films retain tensile strain of comparable magnitude, despite the overall lattice contraction in the target film.

To evaluate the effect of the CsCl interlayer on the moisture resistance of $FAPbI_3$ films, XRD analysis was performed at three stages: pristine film, the film after humidity exposure at 82-88% RH, and the film after post-exposure annealing at 170 °C intended to restore the α-phase from the humidity-induced δ-phase. The relative humidity was set to 82%-88% RH, close to the 85% RH specified in the ISOS-D-3 damp-heat protocol[44,45]. Figure 3 presents the structural degradation and subsequent recovery of the (001)-oriented control and target $FAPbI_3$ films, alongside the corresponding optical images. As shown in Figure 3A, the control film exhibited a substantial decrease in the (001) diffraction intensity after humidity exposure, accompanied by the evolution of the δ-phase and pronounced PbI_2 peaks, consistent with the black-to-yellow color change of the film. Unlike $MAPbI_3$, whose degradation under humid conditions is often associated with hydrate phase formation[46], the degradation of $FAPbI_3$ has more commonly been described in terms of the α-to-δ phase transition and decomposition into FAI and PbI_2[10]. A quantitative comparison of the α-phase, δ-phase, and PbI_2 peak intensities across the three stages is shown in Supplementary Figure 8. Diffraction peaks corresponding to both δ-phase and PbI_2 emerged after humidity exposure [Supplementary Figure 8B and C], indicating that degradation proceeded through both pathways. Although the post-exposure annealing eliminated the humidity-induced δ-phase [Figure 3A and Supplementary Figure 8B], the α-phase barely recovered and the control films turned white, indicating irreversible degradation driven by

the combined effect of moisture and thermal stress. The buried interface typically hosts a high density of defects - oxygen vacancies, hydroxyl groups, iodide vacancies, and undercoordinated Pb sites - that readily trap water molecules under humid conditions and accelerate interfacial degradation[14,36,47], as evidenced in Supplementary Figure 9. The $FAPbI_3$ film deposited on the SnO_2-coated FTO substrate (control film) showed poor moisture resistance during humidity exposure and underwent further irreversible conversion during the post-exposure annealing [Supplementary Figure 9A], whereas both processes were largely suppressed in the film grown on the bare FTO substrate [Supplementary Figure 9B]. Figure 3B shows the corresponding stages for the target film. The initial (001) intensity is higher than that of the control, consistent with the role of CsCl in promoting preferential (001) orientation during growth[29,48-50]. Despite the apparent reduction of the (001) peak during humidity exposure and the emergence of δ-phase and PbI_2 peaks, as also seen in the control film, the target film retained considerable (001) intensity, indicating that the CsCl interlayer improves the moisture tolerance of $FAPbI_3$ films. Remarkably, the target film partially restored the α-phase from the humidity-induced δ-phase during the post-exposure annealing. However, full recovery was not achieved despite complete removal of the δ-phase during the post-exposure anneal. In Supplementary Figure 10, several metal halides were incorporated as an interlayer and examined in the same manner to separate the individual contributions of Cs^+ and Cl^-. The choice of interlayer altered the crystallinity of the overlying perovskite film, and the metal chlorides (NaCl, KCl, and CsCl) gave better crystallinity than the metal iodide (CsI). Although the α-phase recovery is less pronounced than in the CsCl-based target films, these interlayers still produce a partial recovery during the post-exposure annealing [Supplementary Figure 11], suggesting that metal halide interlayers reduce oxygen-vacancy-related defects at the SnO_2 interface, albeit to differing extents depending on the interlayer, and suppress moisture-induced interfacial degradation. This interlayer-driven effect is distinct from the benefit typically attributed to high bulk crystallinity[51,52], as evidenced by the pronounced (001) peak loss in Supplementary Figure 12. When CsCl was instead introduced as a precursor additive, its effect on crystal growth was more pronounced, yielding a sharper (001) peak than that of the target film. After humidity exposure, however, the (001) intensity dropped sharply, confirming that the moisture stability of the target film originates primarily from interfacial effects rather than from bulk crystallinity, although the CsCl-induced improvement in bulk crystallinity still makes a smaller contribution. The structural resilience to moisture therefore appears to be maximized by synergistic effects of passivation of the SnO_2 surface through interlayer coordination and improved crystallinity of the overlying perovskite film, with the CsCl interlayer showing a more pronounced synergistic effect than the independent effects of Cs^+ or Cl^-.

$FAPbI_3$ consists of a corner-sharing $[PbI_6]^{4-}$ octahedral framework, with organic FA^+ cations occupying the cuboctahedral cavities and coupling to the inorganic cage through a combination of ionic and noncovalent interactions[7]. Under moisture exposure, water preferentially hydrogen-bonds to FA^+[53], destabilizing the N-H···I interaction and weakening the FA^+-$[PbI_6]^{4-}$ coupling. FT-IR spectroscopy was performed at the three sequential stages to track the molecular bonding environment within the perovskite lattice. For both the control and target pristine films [Figure 4], the characteristic FA^+ vibrational features appear at 3,400-3,200 cm^{-1}, ~1,712 cm^{-1}, and ~1,354 cm^{-1}, corresponding to the N-H stretching, C=N stretching, and C-H vibrational modes, respectively[54]. Quantitative analysis of the N-H stretching peak is shown in Supplementary Figure 13. For the control sample, the N-H stretching mode showed pronounced broadening and attenuated intensity to ~36.4% of its pristine value after humidity exposure [Figure 4B and Supplementary Figure 13A], indicating that the original N-H···I interactions within the FA^+-$[PbI_6]^{4-}$ sublattice were substantially disrupted, likely through the formation of strong H_2O···FA^+ hydrogen bonds. The C=N-related vibrational peak, by contrast, remained largely intact after humidity exposure, confirming that the FA^+ molecular backbone itself was preserved. Even after post-exposure annealing, the FA^+-$[PbI_6]^{4-}$ interaction was barely restored but rather further weakened, to ~25.5% of the pristine value, suggesting that the FA^+ cations remained preferentially bound to H_2O rather than the inorganic cage. In contrast, the target sample

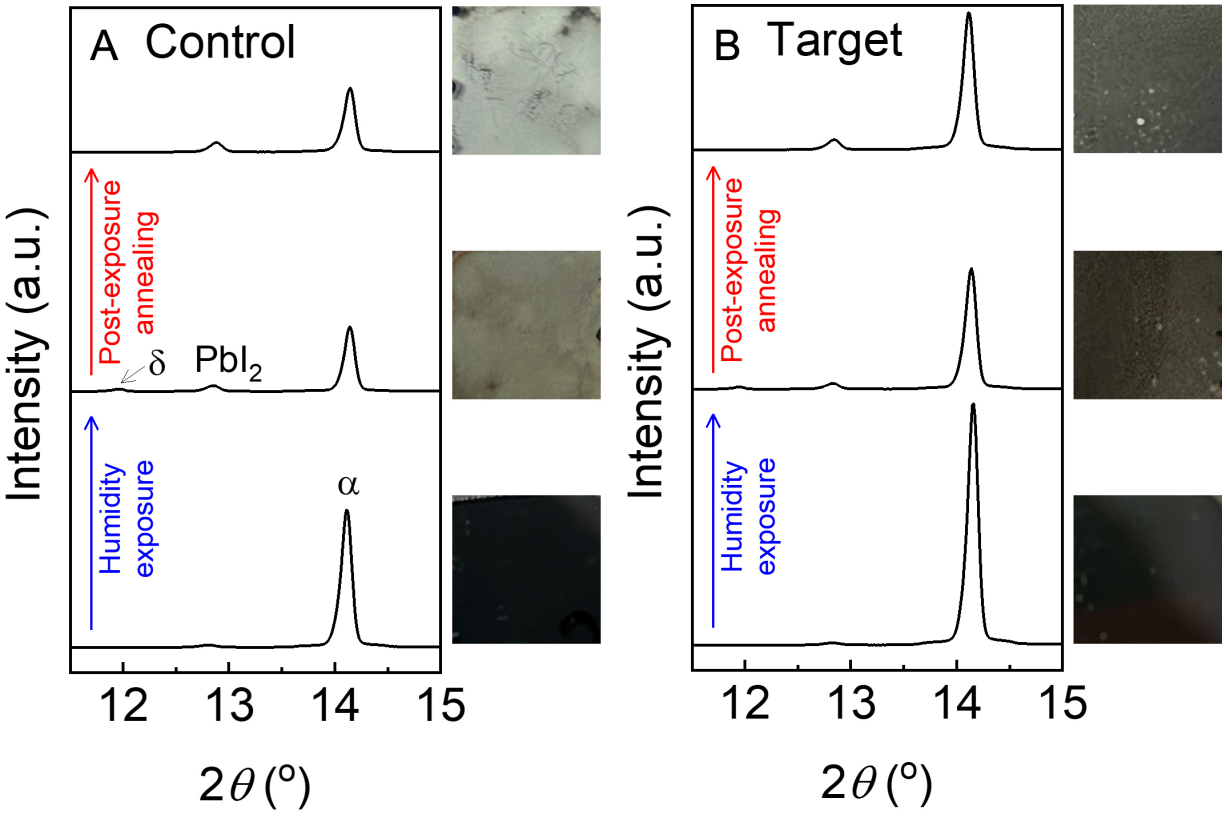

Figure 3. Evolution of XRD patterns for the (A) control and (B) target films at three stages: pristine (bottom), humidity-exposed (middle), and post-exposure annealed (top). Humidity exposure was performed at 82%-88% RH for 30 min, followed by post-exposure annealing at 170 °C for 10 min. XRD: X-ray diffraction; RH: relative humidity.

retained more than 55.6% of its pristine N-H intensity throughout the humidity exposure and post-exposure annealing [Figure 4D and Supplementary Figure 13B]. The CsCl-induced stabilization of the buried interface, which would otherwise act as a preferential adsorption and trapping site for H_2O molecules[12], suppressed moisture accumulation at this defect-rich region, thereby preserving a pristine-like N-H···I bonding environment within the FA^+-$[PbI_6]^{4-}$ framework. In addition to the interfacial effect, Cs^+-induced α-phase stabilization may also contribute to maintaining the FA^+-$[PbI_6]^{4-}$ interaction to some extent[22,52], as pointed out earlier.

Moisture-induced degradation of perovskite films typically proceeds via water adsorption at the film surface, diffusion through grain boundaries, and accumulation at the hydrophilic buried interface[14,55], which is widely considered as the most defect-rich region of n-i-p-structured PSCs[56]. Water desorption from this interface requires relatively high energy (~0.70 eV)[12] due to strong interactions with the surrounding defect sites, indicating direct binding of H_2O to Pb- and I-related defects on the perovskite side and to O-related sites on the SnO_2 surface during moisture-induced phase degradation of $FAPbI_3$. XPS was therefore performed to track changes in the chemical state of the control and target films at three sequential stages. Supplementary Figure 14 shows the depth-resolved XPS profiles of the I $3d_{5/2}$ peak. The control sample exhibited a clear depth dependence of the I $3d_{5/2}$ binding energy after post-exposure annealing [Supplementary Figure 14A], whereas the target film showed only minimal binding-energy shifts across all three stages and across the full depth range [Supplementary Figure 14B]. The largest binding-energy change in the control sample appeared at a depth of 400 nm, near the buried interface, confirming that humidity-induced degradation during the post-exposure annealing was driven primarily by moisture accumulated at

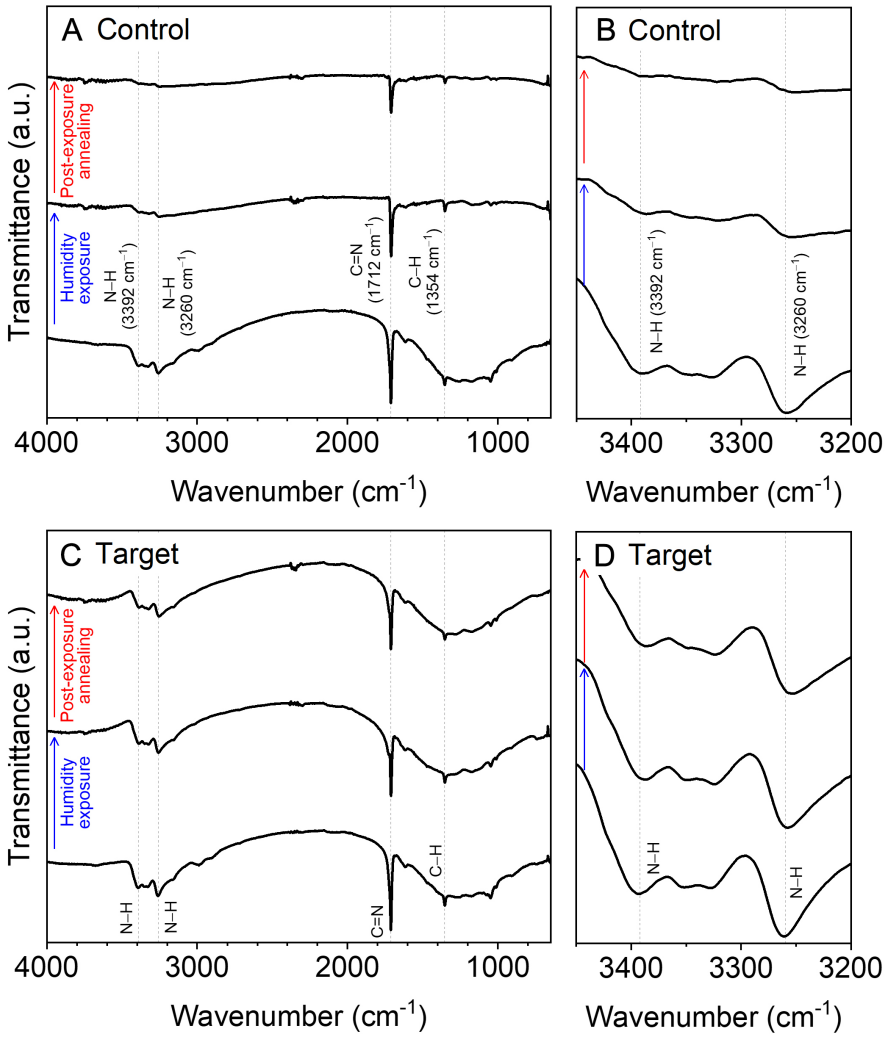

Figure 4. FT-IR spectra of the (A and B) control and (C and D) target $FAPbI_3$ films at three stages: pristine (bottom), humidity-exposed (middle), and post-exposure annealed (top). Panels (A) and (C) show the full spectral range while panels (B) and (D) show enlarged spectra of the N-H stretching region. FT-IR: Fourier-transform infrared.

this interface. XPS spectra of the I $3d_{5/2}$ and O 1s peaks near the buried interface are shown in Figure 5, with dashed guidelines indicating the pristine binding-energy positions. The I $3d_{5/2}$ envelopes [Figure 5A and B] were deconvoluted into two components at each stage: I^- in $FAPbI_3$ lattice (red, 618.74 eV) and I^- in PbI_2 (blue, 619.32 eV)[57,58]. In the pristine stage, the target film showed a higher $FAPbI_3/PbI_2$ ratio than the control, consistent with its higher crystallinity. The coexistence of PbI_2 with $FAPbI_3$ in both pristine films is also supported by a weak PbI_2 XRD peak [Figure 2A] and by the white PbI_2 flakes visible in the surface SEM images (Figure 2B, inset)[59]. Upon humidity exposure, moisture accelerated the transition to the δ-phase (Eq. 1)[10,12], while both samples produced additional PbI_2 via partial $FAPbI_3$ decomposition (Eq. 2), accompanied by a shift of the I $3d_{5/2}$ peak toward lower binding energy. This shift indicates weakening of the Pb-I bonding in the $[PbI_6]^{4-}$ framework[18,60], likely producing a defect-rich buried interface populated by I- and Pb-related defects[61]. In contrast, post-exposure annealing drove the two samples in opposite directions. In the control film, the post-exposure annealing further accelerated $FAPbI_3$ phase degradation. A new component appeared at ~620.1 eV, assigned to iodine in a less electron-rich environment than PbI_2 near vacancy and defect states[61-63], and PbI_2 content increased at the expense of $FAPbI_3$. The thermal release of volatile iodine-related species generates oxidized iodine and modified iodine coordination environments (Eqs. 3-6)[11,57,64]. In the target film, the trend was reversed. The $FAPbI_3$ phase partially recovered while the

PbI_2 content decreased. Even when the $FAPbI_3$ lattice is weakened and partially decomposed by moisture, residual FA^+ species retained within the film recombine with PbI_2 during the post-exposure annealing to restore $FAPbI_3$ (Eq. 7)[65-67]. Supplementary Figure 15 shows a similar but weaker trend in the I $3d_{5/2}$ spectra at a depth of 200 nm, further confirming that the buried interface is the dominant site of moisture-induced degradation. Figure 5C and D show the O 1s spectra deconvoluted into components corresponding to different chemical states. In the pristine films, the dominant component at 530.21 eV is assigned to SnO_2, with additional components from SnO at 529.49 eV, and Sn-OH/chemisorbed oxygen at 530.93 eV[68]. The SnO and Sn-OH components reflect defect-related Sn^{2+} centers and surface hydroxylation at the SnO_2 layer[69]. Upon humidity exposure [Figure 5C], the SnO_2 component shifted toward higher binding energy, accompanied by partial reduction of SnO_2 and a simultaneous increase in the SnO component. These changes indicate that moisture accumulation at the buried interface alters the local chemical environments within SnO_2 and increases the population of defect-related Sn^{2+} sites. Post-exposure annealing of the humidity-exposed control film promoted a new reaction without inducing reconversion into α-phase. At 170 °C, the interfacial oxygen became mobile and reacted with uncoordinated Pb at the buried interface to form Pb-O-related species (Eqs. 4-6). This interfacial oxygen comprises residual H_2O and -OH groups trapped at the interface together with reactive surface oxygen from the SnO_2 layer[65,70,71]. Since the annealing was performed in ambient air, atmospheric oxygen can additionally oxidize mobile iodide, providing a parallel route to the same oxidized products. The co-presence of oxygen and moisture is known to aggravate the degradation of FA- and I-based perovskites, where surface I^- is oxidized to IO_3^-, which subsequently forms $Pb(IO_3)_2$-related products (Eq. 6)[11,72,73]. Such iodate species are consistent with the oxidized iodine component resolved in Figure 5A, and their formation ultimately prevents recovery of the original Pb-I framework[11]. The resulting Pb-O-related species are stable under ambient conditions, and barely reverse to Pb-I[61], indicating that the post-exposure annealing of the humidity-exposed control film drives an irreversible decomposition of $FAPbI_3$. By contrast, the target film suppressed the formation of Pb-O-related species, and the SnO_2 binding energy remained constant across all stages. This indicates that the CsCl interlayer passivates the SnO_2 surface and blocks the irreversible reaction that produces Pb-O-related species during post-exposure annealing, thereby preserving the pathways for reconversion to the α-phase from PbI_2/FAI (Eq. 7) and from δ-phase (Eq. 8)[74,75].

[Humidity exposure (H_2O accumulation at the SnO_2 surface)]

$$\alpha FAPbI_3 \xrightarrow[H_2O]{} \delta FAPbI_3 \tag{1}$$

$$FAPbI_3 \xrightarrow[H_2O]{} PbI_2 + FAI_{(aq)} \tag{2}$$

[Post-exposure annealing under a locally H_2O-rich environment (as in the control film)]

$$FAI + 2H_2O \xrightarrow[\Delta]{} HCOOH + 2NH_3 + HI \tag{3}$$

$$PbI_2 + H_2O \xrightarrow[\Delta]{} Pb(OH)I + HI \tag{4}$$

$$2PbI_2 + 2H_2O + O_2 \xrightarrow[\Delta]{} 2Pb(OH)_2 + 2I_2 \tag{5}$$

$$PbI_2 + 3O_2 \xrightarrow[\Delta]{} Pb\,(IO_3)_2 \tag{6}$$

[Post-exposure annealing under a locally H_2O-poor environment (as in the target film)]

$$PbI_2 + FAI_{(aq)} \xrightarrow[\Delta]{} FAPbI_3 \tag{7}$$

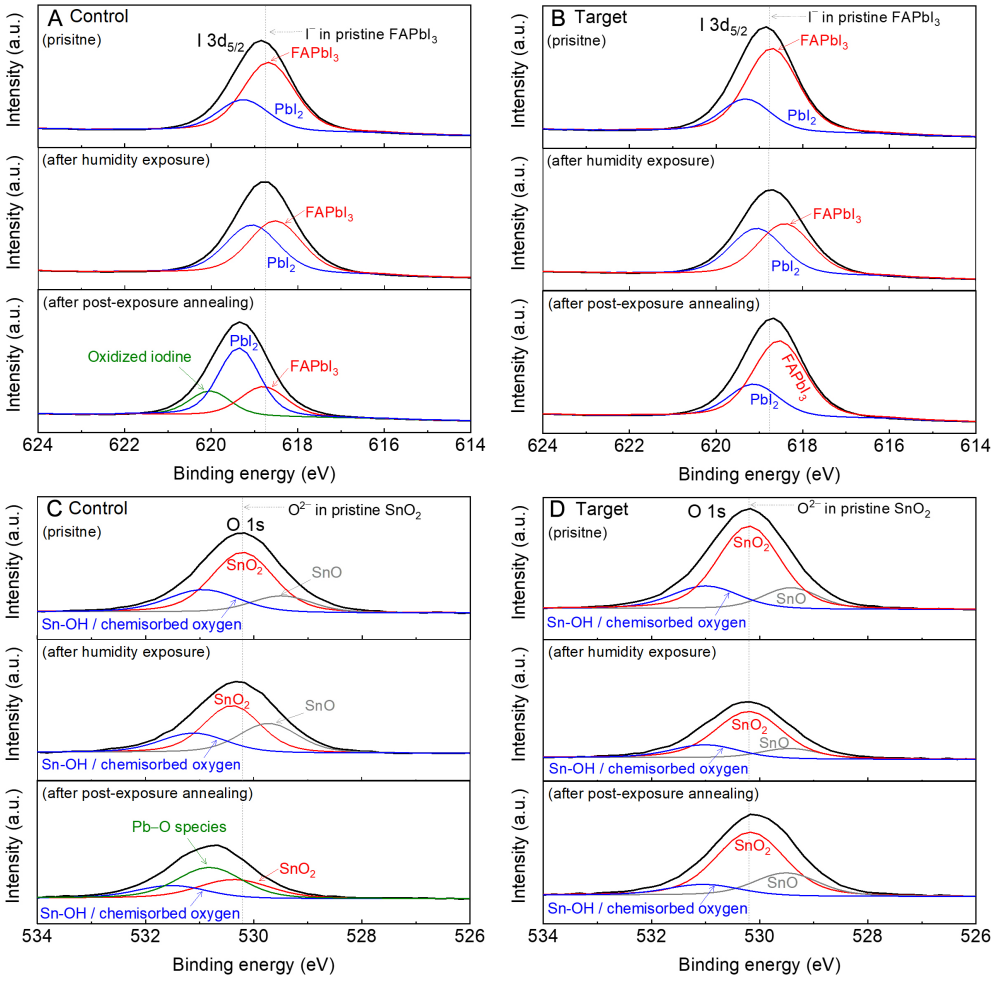

Figure 5. I $3d_{5/2}$ XPS spectra of the (A) control and (B) target films, with dashed lines indicating I^- in the pristine $FAPbI_3$ lattice. O 1s XPS spectra of the (C) control and (D) target films, with dashed lines indicating O^{2-} in the pristine SnO_2 lattice. The I $3d_{5/2}$ XPS spectra were acquired at a depth of 400 nm, corresponding to the overlying $FAPbI_3$ region near the buried interface, whereas the O 1s spectra were acquired at a depth of 600 nm, corresponding to the underlying SnO_2 region near the buried interface. All spectra were collected at each of the three sequential stages. XPS: X-ray photoelectron spectroscopy.

$$\delta FAPbI_3 \underset{\Delta}{\rightarrow} \alpha FAPbI_3 \tag{8}$$

Supplementary Figure 16 shows the Pb $4f_{7/2}$ spectrum at a depth of 400 nm, near the buried interface, and Supplementary Figure 17 shows the corresponding spectrum at a depth of 200 nm, within the bulk of the perovskite film. In both spectra, an additional peak appears at higher binding energy than the PbI_2 component (~139.1 eV)[76,77]. Pb-O-related species such as $Pb(OH)_2$, $PbCO_3$, and $Pb(IO_3)_2$ are known to form during degradation of the analogous perovskite system in conjunction with metal oxide layers[70,71,78], and typically appear at higher binding energy than PbI_2, supporting the assignment of the new O 1s peak in Figure 5C to Pb-O-related species[64,79]. Supplementary Figure 18 accordingly summarizes the depth-dependent XPS profiles of the Pb $4f_{7/2}$ region, in which a substantial shift in binding energy appears only in the control sample after the post-exposure annealing and grows progressively on approaching the buried interface at greater depth. This again points to the buried interface, rather than the bulk perovskite, as the main driver of the irreversible reaction during the post-exposure annealing. Overall, deconvolution of the Pb $4f_{7/2}$, I $3d_{5/2}$, and O 1s spectra near the buried interface in Supplementary Figure 19 provides quantitative support for the mechanism proposed above. In the control sample, the $FAPbI_3$-related components declined as the PbI_2 components grew during the humidity exposure, and the post-exposure annealing converted the PbI_2 together with the Sn-OH/chemisorbed oxygen into Pb-O-related species, consistent across all three core

levels [Supplementary Figure 19A-C]. The portion of Sn-OH/chemisorbed oxygen in O 1s is higher for the control film than for the target film throughout the series, from the pristine film to the humidity-exposed film and the post-exposure annealed film [Supplementary Figure 19C and F], supporting the water-blocking effect of the CsCl interlayer. The target sample followed neither pathway to completion, forming no Pb-O-related species and partially recovering its $FAPbI_3$ signal after the post-exposure annealing relative to the humidity-exposed state [Supplementary Figure 19D-F]. ToF-SIMS was additionally performed to cross-check the formation of Pb-O-related species with and without the CsCl interlayer. In Supplementary Figure 20, ToF-SIMS after post-exposure annealing revealed PbO^- fragments from both samples, with a markedly more intense signal near the buried interface in the control sample. The primary ion beam can itself generate PbO^- during sputtering[80-82]. Because this artifact should be comparable for both samples, it cannot account for the excess observed in the control film. Pb-O-related species therefore formed extensively in the control film but not in the target film during post-exposure annealing. Furthermore, because the Pb-O products are typically amorphous, their formation is consistent with the absence of an additional crystalline phase in the XRD patterns in Figure 3[78]. Consistently, Pb-O-related species increased appreciably only after post-exposure annealing, indicating that the annealing step, rather than the humidity exposure itself, is the kinetic trigger for the irreversible reaction. The elevated temperature accelerates iodide migration, Pb-I bond dissociation, and the transport of oxygen- and hydroxyl-related species[83-85], thereby supplying both the undercoordinated Pb sites and the mobile reactants required for the reactions. The XPS results are consistent with the ToF-SIMS, XRD, and FT-IR trends, demonstrating the resilience afforded to $FAPbI_3$ by the CsCl interlayer at the buried interface, which suppresses the moisture- and thermally driven irreversible decomposition of $FAPbI_3$ into Pb-O-related species.

CONCLUSION

CsCl was introduced as an interlayer at the SnO_2/$FAPbI_3$ buried interface to probe humidity- and thermally driven degradation in n-i-p-structured PSCs. The CsCl interlayer passivated defects at the buried interface and modulated $FAPbI_3$ crystal growth, yielding higher photovoltaic performance with the largest gains in V_{OC}. Beyond the efficiency improvement, CsCl reinforced the structural resilience of $FAPbI_3$ against humidity-induced thermal degradation, a pathway initiated by moisture accumulation at the buried interface. Humidity exposure weakened the Pb-I framework through preferential H_2O interaction with FA^+, generating the δ-phase and PbI_2. In the absence of the CsCl interlayer, subsequent thermal treatment then drove an irreversible reaction in which uncoordinated Pb reacted with surface oxygen at the buried interface to form Pb-O-related species. By contrast, the CsCl-treated interface suppressed Pb-O-related species formation and drove partial reconversion of the δ-phase and PbI_2 to the α-phase during post-exposure annealing. Beyond its interfacial role, the CsCl layer acted synergistically by releasing Cs^+ into the perovskite lattice, where Cs^+-$[PbI_6]^{4-}$ coordination strengthens local bonding and suppresses structural distortion under environmental stress. In conclusion, the CsCl interlayer (i) promotes favorable $FAPbI_3$ crystallization in the pristine film, (ii) mitigates moisture-assisted disruption of the FA^+-$[PbI_6]^{4-}$ sublattice, and (iii) enables partial reconversion of the moisture-induced δ-phase and PbI_2 back to the α-phase while blocking the irreversible degradation pathway to Pb-O-related species at the SnO_2/$FAPbI_3$ buried interface during post-exposure annealing. These findings establish interface-engineered structural resilience as a practical design strategy for $FAPbI_3$-based PSCs.

DECLARATIONS

Authors' Contributions

Data analysis and interpretation, and curation: Lee, G. H.; Kim, H. S.
Writing (original draft), investigation and experiments: Lee, G. H.
Writing (review and editing), conceptualization, supervision, and funding acquisition: Kim, H. S.

Availability of data and materials

The data supporting the findings of this study are available within this Article and its Supplementary Materials. Further data are available from the corresponding authors upon request.

AI and AI-assisted tools statement

Not applicable.

Financial support and sponsorship

This work was supported by the Korea Institute for Advancement of Technology (KIAT No. P0026100).

Conflicts of interest

All authors declared that there are no conflicts of interest.

Ethical approval and consent to participate

Not applicable.

Consent for publication

Not applicable.

Supplementary Materials

Supplementary Materials

REFERENCES

1. Kim, H. S.; Lee, C. R.; Im, J. H.; et al. Lead iodide perovskite sensitized all-solid-state submicron thin film mesoscopic solar cell with efficiency exceeding 9%. *Sci. Rep.* **2012**, *2*, 591. DOI PubMed PMC
2. National Laboratory of the Rockies. Best research-cell efficiency chart. https://www.nlr.gov/pv/cell-efficiency (accessed 2026-09-15).
3. Wu, J.; Yu, S.; Luo, Z.; et al. Approaching 26% efficiency in inverted $FAPbI_3$ perovskite solar cells enabled by tailored fluoropyridine derivative additives. *Adv. Funct. Mater.* **2026**, *36*, e26679. DOI
4. Zheng, Z.; Wang, S.; Hu, Y.; Rong, Y.; Mei, A.; Han, H. Development of formamidinium lead iodide-based perovskite solar cells: efficiency and stability. *Chem. Sci.* **2022**, *13*, 2167-83. DOI PubMed PMC
5. Baltakesmez, A. $FAPbI_3$ perovskite thin film having α/δ phase junction and its light harvesting performance in solar cell. *J. Mater. Sci. Mater. Electron.* **2020**, *31*, 17773-83. DOI
6. Kim, H.; Park, N. Soft lattice and phase stability of α-$FAPbI_3$. *Adv. Energy. Mater.* **2025**, *15*, 2400089. DOI
7. Kim, H. S.; Lee, J. W.; Hagfeldt, A.; Grätzel, M.; Park, N. G. Molecular-level understandings and device strategies for $FAPbI_3$-based perovskite solar cells. *Chem. Soc. Rev.* **2025**, *54*, 11061-88. DOI
8. Zheng, X.; Wu, C.; Jha, S. K.; Li, Z.; Zhu, K.; Priya, S. Improved phase stability of formamidinium lead triiodide perovskite by strain relaxation. *ACS. Energy. Lett.* **2016**, *1*, 1014-20. DOI
9. Chen, S.; Solanki, A.; Pan, J.; Sum, T. C. Compositional and morphological changes in water-induced early-stage degradation in lead halide perovskites. *Coatings* **2019**, *9*, 535. DOI
10. Yun, J. S.; Kim, J.; Young, T.; et al. Humidity-induced degradation via grain boundaries of $HC(NH_2)_2PbI_3$ planar perovskite solar cells. *Adv. Funct. Mater.* **2018**, *28*, 1705363. DOI
11. Hidalgo, J.; Kaiser, W.; An, Y.; et al. Synergistic role of water and oxygen leads to degradation in formamidinium-based halide perovskites. *J. Am. Chem. Soc.* **2023**, *145*, 24549-57. DOI
12. Lee, S.; Lee, D.; Choi, S.; et al. Accelerated degradation of $FAPbI_3$ perovskite by excess charge carriers and humidity. *Solar. RRL.* **2024**, *8*, 2300958. DOI
13. Khan, D.; Muhammad, I.; Qu, G.; et al. Unraveling the reasons behind SnO_2/perovskite defects and their cure through multifunctional $Ti_3C_2T_x$. *Adv. Funct. Mater.* **2024**, *34*, 2316169. DOI
14. Li, N.; Pratap, S.; Körstgens, V.; et al. Mapping structure heterogeneities and visualizing moisture degradation of perovskite films with nano-focus WAXS. *Nat. Commun.* **2022**, *13*, 6701. DOI PubMed PMC
15. Park, S. Y.; Zhu, K. Advances in SnO_2 for efficient and stable n-i-p perovskite solar cells. *Adv. Mater.* **2022**, *34*, e2110438. DOI PubMed

16. Chen, P.; Chen, X.; Du, Y.; et al. Flexible alicyclic ammonium induced bifacial defect passivation for efficient and operationally stable perovskite solar cells. *Small* **2025**, *21*, e06782. DOI
17. Santarossa, G.; Hahn, K.; Baiker, A. Free energy and electronic properties of water adsorption on the SnO_2(110) surface. *Langmuir* **2013**, *29*, 5487-99. DOI PubMed
18. Zhang, J.; Xie, C.; Li, G.; et al. Effect of cation replacement on the phase stability of formamidinium lead iodide perovskite. *J. Chem. Phys.* **2019**, *151*, 134104. DOI
19. Lee, J. H.; Lee, S.; Kim, T.; et al. Interfacial α-$FAPbI_3$ phase stabilization by reducing oxygen vacancies in SnO_{2-x}. *Joule* **2023**, *7*, 380-97. DOI
20. Liang, Y.; Li, F.; Cui, X.; et al. Toward stabilization of formamidinium lead iodide perovskites by defect control and composition engineering. *Nat. Commun.* **2024**, *15*, 1707. DOI PubMed PMC
21. An, Y.; Hidalgo, J.; Perini, C. A. R.; et al. Structural stability of formamidinium- and cesium-based halide perovskites. *ACS. Energy. Lett.* **2021**, *6*, 1942-69. DOI
22. Lee, J.; Kim, D.; Kim, H.; Seo, S.; Cho, S. M.; Park, N. Formamidinium and cesium hybridization for photo- and moisture-stable perovskite solar cell. *Adv. Energy. Mater.* **2015**, *5*, 1501310. DOI
23. Chen, T.; Xie, J.; Wen, B.; et al. Inhibition of defect-induced α-to-δ phase transition for efficient and stable formamidinium perovskite solar cells. *Nat. Commun.* **2023**, *14*, 6125. DOI PubMed PMC
24. Liu, X.; Zhang, Y.; Shi, L.; et al. Exploring inorganic binary alkaline halide to passivate defects in low-temperature-processed planar-structure hybrid perovskite solar cells. *Adv. Energy. Mater.* **2018**, *8*, 1800138. DOI
25. Ji, X.; Bi, L.; Fu, Q.; et al. Target therapy for buried interface enables stable perovskite solar cells with 25.05% efficiency. *Adv. Mater.* **2023**, *35*, e2303665. DOI
26. Jung, E. H.; Chen, B.; Bertens, K.; et al. Bifunctional surface engineering on SnO_2 reduces energy loss in perovskite solar cells. *ACS. Energy. Lett.* **2020**, *5*, 2796-801. DOI
27. Zhu, P.; Gu, S.; Luo, X.; et al. Simultaneous contact and grain-boundary passivation in planar perovskite solar cells using SnO_2-KCl composite electron transport layer. *Adv. Energy. Mater.* **2020**, *10*, 1903083. DOI
28. Adam, I. M.; Soe, K. T.; Ruengsrisang, W.; et al. SnO_2/perovskite interface engineering with mixed-halide potassium salts: a pathway to efficient and stable perovskite solar cells through a combined experimental-density functional theory approach. *ACS. Appl. Mater. Interfaces.* **2025**, *17*, 31000-12. DOI
29. Tang, X.; Chen, M.; Jiang, L.; Li, M.; Tang, G.; Liu, H. Improvements in efficiency and stability of perovskite solar cells using a cesium chloride additive. *ACS. Appl. Mater. Interfaces.* **2022**, *14*, 26866-72. DOI
30. Yang, I. S.; Park, N. Dual additive for simultaneous improvement of photovoltaic performance and stability of perovskite solar cell. *Adv. Funct. Mater.* **2021**, *31*, 2100396. DOI
31. Škorjanc, V.; Miaskiewicz, A.; Roß, M.; et al. Seed layers for wide-band gap coevaporated perovskite solar cells: CsCl regulates band gap and reduces process variability. *ACS. Energy. Lett.* **2024**, *9*, 5639-46. DOI
32. Li, W.; Li, J.; Niu, G.; Wang, L. Effect of cesium chloride modification on the film morphology and UV-induced stability of planar perovskite solar cells. *J. Mater. Chem. A.* **2016**, *4*, 11688-95. DOI
33. Lee, D. K.; Fykouras, K.; Kodalle, T.; et al. Strain engineering: reduction of microstrain at the perovskite surface via alkali metal chloride treatment enhances stability. *ACS. Energy. Lett.* **2025**, *10*, 1039-49. DOI PubMed PMC
34. Jo, N.; Hong, Y.; Yang, S.; Kim, H. Effect of UV-ozone treatment for KCl interlayer in perovskite solar cells. *Bulletin. Korean. Chem. Soc.* **2024**, *45*, 570-5. DOI
35. Chen, B.; Rudd, P. N.; Yang, S.; Yuan, Y.; Huang, J. Imperfections and their passivation in halide perovskite solar cells. *Chem. Soc. Rev.* **2019**, *48*, 3842-67. DOI
36. Saidaminov, M. I.; Kim, J.; Jain, A.; et al. Suppression of atomic vacancies via incorporation of isovalent small ions to increase the stability of halide perovskite solar cells in ambient air. *Nat. Energy.* **2018**, *3*, 648-54. DOI
37. Choi, H. S.; Kim, Y. N.; Hong, S.; et al. Oriented crystal growth during perovskite surface reconstruction. *ACS. Appl. Mater. Interfaces.* **2022**, *14*, 51149-56. DOI
38. Cho, C.; Feldmann, S.; Yeom, K. M.; et al. Efficient vertical charge transport in polycrystalline halide perovskites revealed by four-dimensional tracking of charge carriers. *Nat. Mater.* **2022**, *21*, 1388-95. DOI
39. Liu, S.; Peng, H.; Yang, Y.; et al. KCl induces a “slow-release effect” on PbI_2 to strengthen the crystallization of perovskite and the reverse-bias stability of carbon-electrode-based solar cells. *J. Mater. Chem. C.* **2025**, *13*, 16159-71. DOI
40. Hou, M.; Wang, Y.; Han, M.; et al. Potassium chloride templated α-$FAPbI_3$ perovskite crystal growth for efficient planar perovskite solar cells. *Organic. Electronics.* **2022**, *106*, 106527. DOI

41. Rehman, W.; Mcmeekin, D. P.; Patel, J. B.; et al. Photovoltaic mixed-cation lead mixed-halide perovskites: links between crystallinity, photo-stability and electronic properties. *Energy. Environ. Sci.* **2017**, *10*, 361-9. DOI
42. Gao, L.; Zhang, F.; Chen, X.; et al. Enhanced charge transport by incorporating formamidinium and cesium cations into two-dimensional perovskite solar cells. *Angew. Chem. Int. Ed.* **2019**, *58*, 11737-41. DOI
43. Yang, B.; Bogachuk, D.; Suo, J.; et al. Strain effects on halide perovskite solar cells. *Chem. Soc. Rev.* **2022**, *51*, 7509-30. DOI PubMed PMC
44. Gallant, B. M.; Holzhey, P.; Smith, J. A.; et al. A green solvent enables precursor phase engineering of stable formamidinium lead triiodide perovskite solar cells. *Nat. Commun.* **2024**, *15*, 10110. DOI PubMed PMC
45. Khenkin, M. V.; Katz, E. A.; Abate, A.; et al. Consensus statement for stability assessment and reporting for perovskite photovoltaics based on ISOS procedures. *Nat. Energy.* **2020**, *5*, 35-49. DOI
46. Jasti, N. P.; Shter, G. E.; Feldman, Y.; et al. The saga of water and halide perovskites: evidence of water in methylammonium lead Tri-iodide. *Adv. Funct. Mater.* **2022**, *32*, 2204283. DOI
47. Ouyang, Y.; Shi, L.; Li, Q.; Wang, J. Role of water and defects in photo-oxidative degradation of methylammonium lead iodide perovskite. *Small. Methods.* **2019**, *3*, 1900154. DOI
48. Zhang, M.; Zhao, T.; Fang, S.; Chen, G. Enhancement of the ultraviolet stability of perovskite solar by the interface modified with cesium chloride. *Adv. Photon. Res.* **2026**, *7*, e202500156. DOI
49. Yang, L.; Xie, J.; Su, Z.; et al. CsCl seed layer engineering for buried-interface modification enabling >20% efficiency in single-source vapor-deposited perovskite solar cells. *J. Mater. Chem. A.* **2026**, *14*, 13462-70. DOI
50. Liu, Y.; He, L.; Chen, X.; Zhang, C.; Cheng, J.; Li, J. Comparative study of cesium halide (CsX, X = I, Cl, Br) modifications on defect passivation in tin-based perovskite solar cells. *J. Appl. Phys.* **2024**, *136*, 023107. DOI
51. Li, Z.; Yang, M.; Park, J.; Wei, S.; Berry, J. J.; Zhu, K. Stabilizing perovskite structures by tuning tolerance factor: formation of formamidinium and cesium lead iodide solid-state alloys. *Chem. Mater.* **2016**, *28*, 284-92. DOI
52. Yi, C.; Luo, J.; Meloni, S.; et al. Entropic stabilization of mixed A-cation ABX_3 metal halide perovskites for high performance perovskite solar cells. *Energy. Environ. Sci.* **2016**, *9*, 656-62. DOI
53. Svane, K. L.; Forse, A. C.; Grey, C. P.; et al. How strong is the hydrogen bond in hybrid perovskites? *J. Phys. Chem. Lett.* **2017**, *8*, 6154-9. DOI PubMed PMC
54. Arjun Suresh, P.; Parvathy, B.; John, G. S.; Johnson, A. M.; Sajeev, U.; Arun Kumar, K. Temperature dependence study of $FAPbI_3$ thin films annealed under controlled humidity and light conditions. *Results. Surf. Interfaces.* **2025**, *21*, 100682. DOI
55. Kim, J.; Jo, W. Engineering of buried interfaces in perovskites: advancing sustainable photovoltaics. *Nano. Converg.* **2024**, *11*, 57. DOI PubMed PMC
56. Huang, L.; Wang, K.; Jin, R.; et al. Reshaped buried interface by comprehensive passivation for highly efficient perovskite photovoltaics. *Chem. Eng. J.* **2024**, *488*, 150815. DOI
57. Salim, K. M. M.; Masi, S.; Gualdrón-Reyes, A. F.; et al. Boosting long-term stability of pure formamidinium perovskite solar cells by ambient air additive assisted fabrication. *ACS. Energy. Lett.* **2021**, *6*, 3511-21. DOI PubMed PMC
58. Rakheja, B.; Hultqvist, A.; Varma, R. M.; et al. Interfacial chemistry between formamidinium lead trihalide perovskites and atomic-layer-deposited tin oxide. *ACS. Appl. Energy. Mater.* **2025**, *8*, 8467-78. DOI
59. Tumen-Ulzii, G.; Qin, C.; Klotz, D.; et al. Detrimental effect of unreacted PbI_2 on the long-term stability of perovskite solar cells. *Adv. Mater.* **2020**, *32*, e1905035. DOI
60. Luo, S.; Cao, S.; Zheng, T.; et al. Melamine holding PbI_2 with three “arms”: an effective chelation strategy to control the lead iodide to perovskite conversion for inverted perovskite solar cells. *Energy. Environ. Sci.* **2025**, *18*, 2436-51. DOI
61. Zhang, H.; Mao, Z.; Ma, Y.; et al. Deciphering thermal degradation pathways of metal halide perovskite thin films under ambient conditions. *J. Colloid. Interface. Sci.* **2025**, *700*, 138341. DOI
62. Wu, W. Q.; Rudd, P. N.; Ni, Z.; et al. Reducing surface halide deficiency for efficient and stable iodide-based perovskite solar cells. *J. Am. Chem. Soc.* **2020**, *142*, 3989-96. DOI
63. Joo Yang, S.; Jin, H.; Cha, J.; et al. Elucidating degradation mechanisms of mixed cation formamidinium-based perovskite solar cells under device operation conditions. *Appl. Surf. Sci.* **2023**, *612*, 155805. DOI
64. Huang, P. C.; Yang, T. J.; Lin, C. J.; Wang, M. Y.; Lin, W. C. Unraveling the heat- and UV-induced degradation of mixed halide perovskite thin films via surface analysis techniques. *Langmuir* **2024**, *40*, 11873-87. DOI PubMed PMC
65. Ho, K.; Wei, M.; Sargent, E. H.; Walker, G. C. Grain transformation and degradation mechanism of formamidinium and cesium lead iodide perovskite under humidity and light. *ACS. Energy. Lett.* **2021**, *6*, 934-40. DOI
66. Bu, T.; Ono, L. K.; Li, J.; et al. Modulating crystal growth of formamidinium-caesium perovskites for over 200 cm^2 photovoltaic sub-modules. *Nat. Energy.* **2022**, *7*, 528-36. DOI

67. Zhang, Y.; Yang, T.; Lee, S.; Liu, S.; Zhao, K.; Park, N. Stabilizing α-phase $FAPbI_3$ perovskite induced by an ordered solvated quasi-crystalline PbI_2. *ACS. Energy. Lett.* **2024**, *9*, 159-67. DOI
68. Kwoka, M.; Ottaviano, L.; Passacantando, M.; Santucci, S.; Czempik, G.; Szuber, J. XPS study of the surface chemistry of L-CVD SnO_2 thin films after oxidation. *Thin. Solid. Films.* **2005**, *490*, 36-42. DOI
69. Batzill, M.; Diebold, U. The surface and materials science of tin oxide. *Prog. Surf. Sci.* **2005**, *79*, 47-154. DOI
70. Huang, W.; Manser, J. S.; Kamat, P. V.; Ptasinska, S. Evolution of chemical composition, morphology, and photovoltaic efficiency of $CH_3NH_3PbI_3$ perovskite under ambient conditions. *Chem. Mater.* **2016**, *28*, 303-11. DOI
71. Wang, C.; Amornkitbamrung, U.; Xu, Y.; et al. Buried interface engineering in metal-halide perovskite/NiO heterostructures through direct observation of interfacial reactions. *ACS. Energy. Lett.* **2026**, *11*, 4580-9. DOI
72. Hartmann, C.; Sadoughi, G.; Félix, R.; et al. Spatially resolved insight into the chemical and electronic structure of solution-processed perovskites-why to (Not) worry about pinholes. *Adv. Mater. Inter.* **2018**, *5*, 1701420. DOI
73. Holland, M.; Ruth, A.; Mielczarek, K.; Dhas, V. V.; Berry, J. J.; Irwin, M. D. Metal halide perovskites demonstrate radiation hardness and defect healing in vacuum. *ACS. Appl. Mater. Interfaces.* **2022**, *14*, 9352-62. DOI PubMed
74. Yang, C.; Chen, C.; Bian, T.; et al. Anisotropic δ-to-α phase transition in formamidinium lead iodide thin films. *ACS. Nano.* **2025**, *19*, 9225-31. DOI PubMed PMC
75. Fu, F.; Pisoni, S.; Jeangros, Q.; et al. I_2 vapor-induced degradation of formamidinium lead iodide based perovskite solar cells under heat-light soaking conditions. *Energy. Environ. Sci.* **2019**, *12*, 3074-88. DOI
76. Hultqvist, A.; Jacobsson, T. J.; Svanström, S.; et al. SnO_x atomic layer deposition on bare perovskite-an investigation of initial growth dynamics, interface chemistry, and solar cell performance. *ACS. Appl. Energy. Mater.* **2021**, *4*, 510-22. DOI
77. Le, D.; Wei, T. In-depth investigation of methylamine gas post-treatment for $MAPbI_3$ films and its potential for upscaling perovskite solar cells. *EES. Sol.* **2026**, *2*, 183-97. DOI
78. Rocks, C.; Svrcek, V.; Maguire, P.; Mariotti, D. Understanding surface chemistry during $MAPbI_3$ spray deposition and its effect on photovoltaic performance. *J. Mater. Chem. C.* **2017**, *5*, 902-16. DOI
79. Bilal, M.; Hameed, M.; Igbari, F.; et al. Insights into degradation pathways of perovskite thin films under outdoor and indoor conditions: a comparative analysis. *Adv. Opt. Mater.* **2026**, *14*, e03613. DOI
80. Harvey, S. P.; Zhang, F.; Palmstrom, A.; Luther, J. M.; Zhu, K.; Berry, J. J. Mitigating measurement artifacts in TOF-SIMS analysis of perovskite solar cells. *ACS. Appl. Mater. Interfaces.* **2019**, *11*, 30911-8. DOI PubMed
81. Sander, P.; Kaiser, U.; Jede, R.; Lipinsky, D.; Ganschow, O.; Benninghoven, A. Secondary ion and sputtered neutral formation from oxygen loaded Si(100). *J. Vac. Sci. Technol. A.* **1985**, *3*, 1946-54. DOI
82. Reuter, W.; Wittmaack, K. An AES-SIMS study of silicon oxidation induced by ion or electron bombardment. *Appl. Surf. Sci.* **1980**, *5*, 221-42. DOI
83. Minns, J. L.; Zajdel, P.; Chernyshov, D.; van Beek, W.; Green, M. A. Structure and interstitial iodide migration in hybrid perovskite methylammonium lead iodide. *Nat. Commun.* **2017**, *8*, 15152. DOI PubMed PMC
84. Aristidou, N.; Eames, C.; Sanchez-Molina, I.; et al. Fast oxygen diffusion and iodide defects mediate oxygen-induced degradation of perovskite solar cells. *Nat. Commun.* **2017**, *8*, 15218. DOI PubMed PMC
85. Zhang, L.; Sit, P. H. Ab initio study of interaction of water, hydroxyl radicals, and hydroxide ions with $CH_3NH_3PbI_3$ and $CH_3NH_3PbBr_3$ surfaces. *J. Phys. Chem. C.* **2015**, *119*, 22370-8. DOI